Materials Advances

ROYAL SOCIETY OF CHEMISTRY

PAPER

View Article Online
View Journal

Open Access Article. Published on 25 November 2025. Downloaded on 1/19/2026 10:11:12 PM.
This article is licensed under a Creative Commons Attribution 3.0 Unported Licence.

Check for updates

Cite this: DOI: 10.1039/d5ma00500k

Structural and thermoelectric properties of $Mn(Si_{1-x}Al_x)_{1.75}$: a commensurate phase mixture approximation

Panagiotis Mangelis, *[a] Panagiotis S. Ioannou,[a] Anne-Karin Søiland[b] and Theodora Kyratsi[a]

Received 16th May 2025,
Accepted 20th November 2025

DOI: 10.1039/d5ma00500k

rsc.li/materials-advances

Higher manganese silicide (HMS) compounds with the nominal stoichiometry of $Mn(Si_{1-x}Al_x)_{1.75}$ ($0 \leq x \leq 0.04$) are synthesized using the arc melting method. Structural investigations are carried out executing powder XRD Rietveld refinements on different models from the Nowotny chimney ladder (NCL) phases. It is revealed that the commensurate two-phase mixture model, based on the $I\bar{4}2d$ $Mn_{15}Si_{26}$ and $P\bar{4}n2$ $Mn_{27}Si_{47}$ superstructures, approximates quite well the modulated structure of the prepared materials with the majority phase as $Mn_{27}Si_{47}$ for $x = 0$. Le Bail analysis enhances the validity of the commensurate approximation, comparing the two-phase mixture with the (3 + 1)D incommensurate structural model with the superspace group $I4_1/amd(00\gamma)00ss$. Al substitution causes expansion of both tetragonal supercells across the z axis, while the a lattice constant is affected marginally. Interestingly, the evolution of the phase fraction across the $Mn(Si_{1-x}Al_x)_{1.75}$ ($0 \leq x \leq 0.04$) series favours the formation of $Mn_{15}Si_{26}$, and a noticeable change occurs at $x = 0.025$, which seems to be correlated with an abrupt variation in the electrical transport properties. Electrical conductivity and Seebeck coefficient measurements show that Al doping induces an effective increase in hole concentration, resulting in a significant increase in σ for $x = 0.025$. An improvement in ZT is achieved with $Mn(Si_{0.975}Al_{0.025})_{1.75}$ phase demonstrating a maximum value close to 0.6 at 773 K. In addition, the replacement of high-purity Si with two types of recycled Si kerf from the PV industry is attempted here to develop HMS phases. Powder XRD and SEM analyses show the existence of an appreciable amount of MnSi in both kerf-based products, strongly affecting their thermoelectric (TE) properties. Although the two kerf-based phases present lower efficiencies, this is the first time p-type silicide thermoelectrics are synthesized *via* the arc melting method using recycled Si, which is quite important for future research.

Introduction

TE devices play an important role in energy savings and waste heat recovery in industrial processes since considerable amount of heat is emitted in the environment globally.[1,2] The operation of a TE device is based on the Seebeck effect, where heat is converted directly into clean electricity without carbon emissions. From the point of view of materials, in order to a achieve a good TE efficiency, a high electrical conductivity (σ) is required, which is characteristic of metallic materials, combined with a high Seebeck coefficient (S) and low thermal conductivity (κ), usually attributed to non-metallic phases. The aforementioned properties are incorporated in the dimensionless figure-of-merit, $ZT = S^2\sigma T/\kappa$, which defines the TE performance.

Commercially available TE materials, which are made of Bi_2Te_3 alloys, demonstrate ZT values around 1 at room temperature.[3] However, the scarcity and high-cost of tellurium hinder their large-scale and cost-efficient applications.[4] In addition, the rapid reduction of ZT at higher temperatures makes these materials unsuitable for intermediate-temperature applications. Considerable research efforts are currently focused on the discovery of Te-free alternatives, environmentally friendly and low-cost materials with optimized TE efficiencies,[5–7] to overcome the challenges in the future commercialization of TE devices.[8] Some of the most promising Te-free material groups, composed of earth-abundant elements, are half-heusler phases,[9] silicides,[10,11] oxides,[12] sulphides[13] and selenides.[14]

HMS phases with the general formula $MnSi_\gamma$ ($1.67 < \gamma < 1.77$) have attracted considerable attention as the most promising p-type thermoelectrics from the group of silicides. HMS are

[a] Department of Mechanical and Manufacturing Engineering, University of Cyprus, 1678 Nicosia, Cyprus. E-mail: mangelis.panagiotis@ucy.ac.cy
[b] ReSiTec AS, Setesdalsveien 110, 4617 Kristiansand, Norway

Open Access Article. Published on 25 November 2025. Downloaded on 1/19/2026 10:11:12 PM.
This article is licensed under a Creative Commons Attribution 3.0 Unported Licence.

intermetallic compounds composed of low-cost, earth-abundant and non-toxic elements, demonstrating good TE properties.[15] In addition, these materials exhibit excellent mechanical, chemical and thermal stability,[16] which make them suitable and promising alternatives to PbTe-based thermoelectrics for mid-temperature applications. They exhibit a high Seebeck coefficient and relatively low resistivity,[17] with the pristine material achieving a *ZT* around 0.4–0.55, depending on its synthesis method.[15]

HMS phases crystallize in NCL structures. Their tetragonal unit cell consists of a Mn sub-lattice with a β-Sn configuration (chimney) in which the Si sub-lattice climbs as a helical ladder.[18,19] Although these structures have similar lattice parameters across the *x* and *y* axes, the slight differences in the silicon sub-lattice lead to different space groups and wide variations in their *c* lattice parameter. As shown in Fig. 1, there are four basic NCL tetragonal phases (Mn_4Si_7, $Mn_{11}Si_{19}$, $Mn_{15}Si_{26}$, and $Mn_{27}Si_{47}$), which have been determined by X-ray diffraction (XRD), while other commensurate phases such as Mn_7Si_{12}, $Mn_{19}Si_{33}$, $Mn_{26}Si_{45}$, and $Mn_{39}Si_{68}$ have also been revealed for HMS.[19] The *c* lattice parameter follows the empirical rule $c = n\cdots c_{Mn} = m\cdots c_{Si}$, where *n* and *m* are integers in the formula Mn_nSi_{2n-m} and define the number of Mn and Si sub-lattices in the unit cell, respectively.[19,20] Among the NCL tetragonal phases, the lattice parameters determined by the Mn sub-lattice, *a* and c_{Mn}, are almost constant, while small variations in the Si sub-lattice and c_{Si} result in superstructures with a significant increase in *c* up to several tens of nanometers.[19] Stability studies have shown that among the aforementioned basic phases, at room temperature and up to 1073 K the stable phase is $Mn_{27}Si_{47}$, while above 1073 K, a phase transition to $Mn_{15}Si_{26}$ takes place.[21,22] Another study suggests that the nominal $MnSi_{1.75}$ phase is crystallized in Mn_4Si_7, which is transformed to $Mn_{11}Si_{19}$ at high temperatures, forming MnSi in parallel.[23] The aforementioned commensurate phases usually coexist, while the presence of MnSi precipitates in the HMS matrix is quite common due to the peritectic reaction of MnSi with Si to form Mn_nSi_{2n-m}.[15,24] It must be noted here that due to the irrational *c*-axis ratio $\gamma = c_{Mn}/c_{Si}$, a large number of independent crystallographic positions of modulated commensurate phases is required to account for the *z*-axis difference.[25] Owing to this, a (3 + 1)-dimensional superspace group approach has been proposed recently for the crystal structure of HMS phases, using the group $I4_1/amd(00\gamma)00ss$.[25–28] Powder neutron diffraction revealed the modulated helical arrangement of Si atoms along the *c* axis, indicating an incommensurate approach for $MnSi_\gamma$ phases with $1.70 \leq \gamma \leq 1.75$.[25] However, the commensurate approximation of modulated phases is necessary for the determination of their electronic structure. In addition, it provides higher precision and simplicity in band structure calculations, avoiding the conversion into 3D space.[25] Band structure calculations have been carried out for the commensurate phases (Mn_4Si_7, $Mn_{11}Si_{19}$, $Mn_{15}Si_{26}$ and $Mn_{27}Si_{47}$) by Migas *et al.*, revealing differences in the density of states near the Fermi level and the semiconducting behaviour of the investigated phases.[29] Slight changes in the Si stoichiometry in $MnSi_\gamma$ appreciably affect their charge carrier concentration, and consequently their TE properties. A synchrotron X-ray diffraction study, investigating the influence of annealing conditions on the modulation vector γ, showed that the thermal history has a strong impact on the stoichiometry of silicon and the TE performance of developed HMS phases.[27]

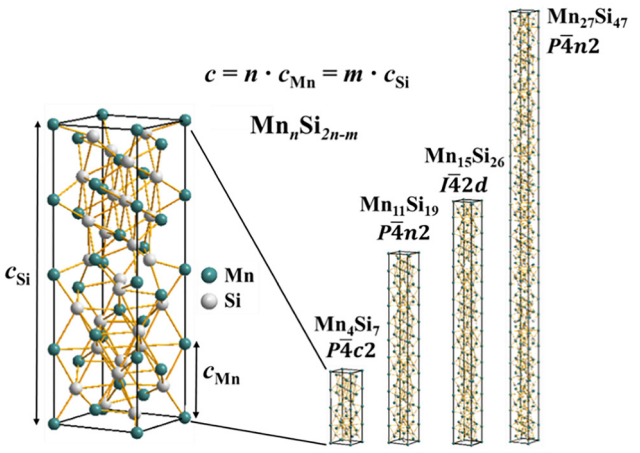

Fig. 1 Illustration of HMS crystal structures corresponding to the four NCL phases.

Many studies have focused on improving the TE performance of HMS phases through appropriate doping to optimize their hole concentration and tune their electrical transport properties. Various chemical substitutions have been attempted either on the Si site with dopants such as Al,[28,30,31] B[32] and Ge[33] or on the Mn site with Cr,[34,35] V,[36] Fe,[37] Ta,[38] and W,[37] targeting an enhancement in *ZT*. Among the non-isoelectronic dopants, Al substitution has shown the most promising TE properties. It is notable that 5 at % Al-doped $MnSi_{1.73}$ prepared *via* melt-spinning and spark plasma sintering (SPS) exhibited a *ZT* of ∼0.82 at 800 K. Multiple substitutions have also been employed with various dopant combinations such as Al/Fe,[39] Al/Ge,[40] Cr/Fe,[35] Cr/Ru,[41] Re/Ge[42] and Mo/W/Al/Ge.[43] Implementing arc melting and the melt-spinning technique, supersaturated Re substitution was achieved in $Mn_{36.4}Si_{63.6}$, resulting in a significant reduction in the lattice thermal conductivity and remarkable *ZT* enhancements with values above 1.[44–46]

Several synthetic techniques have already been employed for the development of HMS phases, which have shown notable variations in TE performance. Melting methods such as melt-spinning,[30,44,47,48] arc melting,[33,35,37,49] melt-quenching[50] and induction melting[51,52] have been proven to be advantageous compared with other techniques in terms of MnSi suppression and expansion of the dopant solubility limits. The existence of the undesirable metallic MnSi phase causes a severe decline in the TE performance of HMS due to the increase in hole concentration,[53] which leads to an appreciable reduction in Seebeck coefficient. In addition, it has been proven that MnSi precipitates are responsible for the increase in lattice thermal conductivity.[54,55] Therefore, the extinction of the MnSi phase is critical for the enhancement in TE properties. Recently, Chauhan *et al.* showed that Al-doped HMS polycrystals developed by melt-spinning and SPS surpass single crystals grown by the

 © 2025 The Author(s). Published by the Royal Society of Chemistry

Open Access Article. Published on 25 November 2025. Downloaded on 1/19/2026 10:11:12 PM.
This article is licensed under a Creative Commons Attribution 3.0 Unported Licence.

Bridgman method, eliminating MnSi and increasing the Al solubility.[28] As a result, the polycrystalline materials exhibited an improved TE efficiency, achieving a ZT of 0.75 at 873 K. Another comparative study on synthetic methods showed that the MnSi phase is notably decreased in the final product by applying the arc melting method instead of solid-state reaction, resulting in an increase in ZT of 15%.[49] Although several studies have used arc melting for the synthesis of HMS phases, quite few have combined this method with hot-press sintering.[41,56,57] Moreover, the environmental challenges related with material recycling and the circular economy[58] have intensified research efforts devoted to the development of thermoelectrics using recycled raw materials in the last few years. Silicide TE materials have the potential to provide an effective sustainable route for the utilization of recycled silicon.[59] Thus far, our investigations on the development of n-type $Mg_2Si_{1-x}Sn_x$ solid solutions based on Si kerf from the PV industry have shown quite promising results.[60–63] However, systematic studies to investigate the development of p-type higher manganese silicides using recycled silicon are quite limited.[64]

In this study, HMS phases of the $Mn(Si_{1-x}Al_x)_{1.75}$ series are developed by arc melting and hot-press sintering. In an attempt to correlate the structural and electronic properties of the developed phases across the $Mn(Si_{1-x}Al_x)_{1.75}$ series, deciphering the effect of Al substitution on the crystal lattice and TE properties, a commensurate approximation is studied, investigating structural models from the NCL phases. The results from powder XRD Rietveld refinements reveal for first time a commensurate two-phase mixture approach for the crystal structure of pristine and Al-doped phases. Its evolution is investigated across the $Mn(Si_{1-x}Al_x)_{1.75}$ ($0 \leq x \leq 0.04$) series and a partial phase transition is revealed with Al substitution, which seems to be correlated with the observed changes in electrical transport properties. Al doping enhances hole concentration, and optimization of the TE performance is achieved in $Mn(Si_{1-x}Al_x)_{1.75}$ ($0 \leq x \leq 0.04$). In an attempt to utilize recycled silicon and expand our investigations on the development of p-type recycled Si based-silicide thermoelectrics, two types of Si kerf from PV manufacturing are used to synthesise Al-doped HMS phases, implementing for first time the arc melting method.

Experimental

Al-doped $MnSi_{1.75}$ phases were synthesized *via* the arc melting method using high-purity and recycled Si. Commercial Si, Mn and Al reagents were supplied by Alfa Aesar with purity greater than 99.9%. Appropriate stoichiometric amounts of the reagent elements in powder form were mixed under an argon atmosphere and cold pressed at 0.5 GPa into pellets. The resulting pellets were melted under an Ar atmosphere, flipped and remelted three times. Ball milling was carried out at 300 rpm for 1 h in a planetary mill (Pulverisette 6, Fritsch) for grinding the final products to fine powders with a homogeneous grain size. Densification of the developed powders into pellets was carried out uniaxially through hot-press sintering under an argon atmosphere at 1000 °C and pressure of 80 MPa for 1 h in an HP20, Thermal Technologies system.

Powder XRD measurements were carried out using a Rigaku SmartLab diffractometer, operating with a Cu-Kα source at 9 kW (45 kV, 200 mA). A scan time of 0.6 s per step and a scan step of 0.02° over the angular range of $20 \leq 2\theta/^\circ \leq 90$ were set. Rietveld refinements were performed using the General Structure Analysis System (GSAS) software package and the ICDD crystallographic information files for the following HMS phases: Mn_4Si_7 (PDF# 04-010-6000), $Mn_{11}Si_{19}$ (PDF# 04-004-6999), $Mn_{15}Si_{26}$ (PDF# 04-007-5322) and $Mn_{27}Si_{47}$ (PDF# 00-026-1251). Le Bail analysis was carried out on powder XRD data using the GSAS-II software package and the (3 + 1)D superspace group $I4_1/amd(00\gamma)00ss$.[25] Scanning electron microscopy (SEM) was used for the micro-structure characterization of the investigated materials. The hot-press sintered pellets were examined using a backscattered electron (BSE) detector. SEM imaging was performed using a Tescan Vega II LSU, thermionic emission electron microscope at an accelerating voltage of 20 kV.

The experimental density of the pellets was calculated using a geometrical method. A ZEM-3 ULVAC-RIKO was employed for electrical conductivity and Seebeck coefficient measurements under a helium atmosphere in the temperature range of $300\ K \leq T \leq 773\ K$. The thermal diffusivity (D) and specific heat capacity (C_p) of the samples were measured using a Netzsch LFA 457 laser setup. Data were collected in 50 K increments on pellets coated with graphite. A pyroceram reference sample was used for C_p measurements. The thermal conductivity was determined using the formula $\kappa = D\rho C_p$. The estimated uncertainties for the measurements of electrical and thermal transport properties are ±5% and ±7%, respectively.

Results and discussion

HMS phases with the general formula $Mn(Si_{1-x}Al_x)_{1.75}$ ($0 \leq x \leq 0.04$) were synthesized using the arc melting method. Material characterization was carried out for all the developed phases using powder XRD. Structural investigations were performed executing Rietveld refinements to determine the structural model among the commensurate NCL phases that most effectively describes the crystal structure of the prepared materials. Hole doping through Al substitution at the silicon site was implemented to tune the electrical transport properties and optimize the TE efficiency. The replacement of commercial silicon with two types of recycled Si kerf is also studied here for the Al-doped phase with the best TE performance.

Structural characterization of $Mn(Si_{1-x}Al_x)_{1.75}$ ($0 \leq x \leq 0.04$)

Powder XRD measurements were performed to investigate the purity of the materials and the existence of possible secondary phases. Fig. 2 shows the XRD patterns of the synthesized phases in the $Mn(Si_{1-x}Al_x)_{1.75}$ ($0 \leq x \leq 0.04$) series. All the investigated products possessed high purity and formed the

Open Access Article. Published on 25 November 2025. Downloaded on 1/19/2026 10:11:12 PM.
This article is licensed under a Creative Commons Attribution 3.0 Unported Licence.

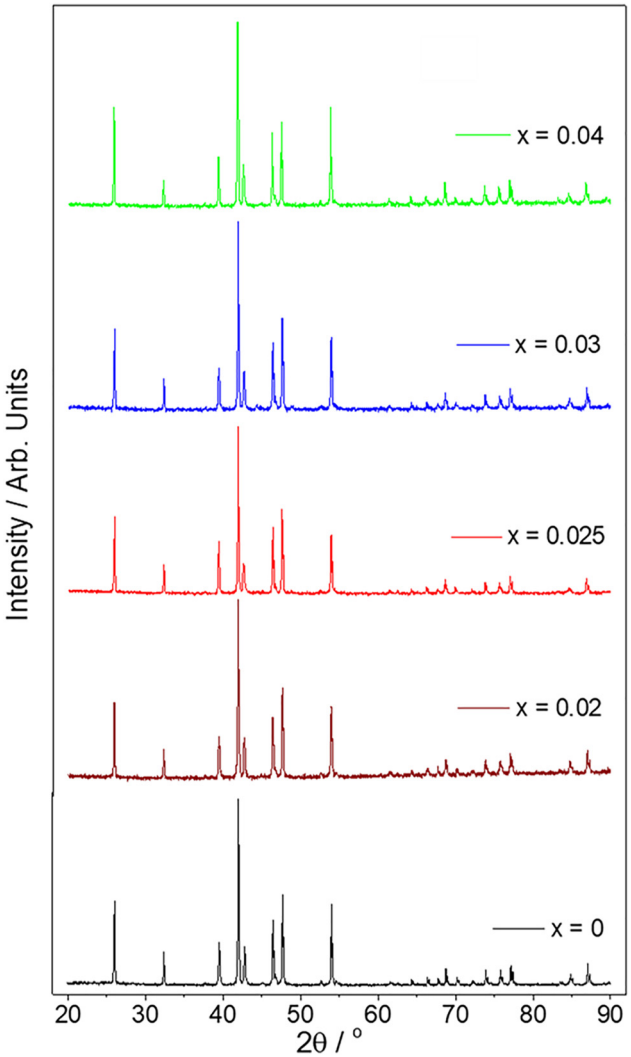

Fig. 2 Powder XRD data in arbitrary units for the $Mn(Si_{1-x}Al_x)_{1.75}$ phases ($0 \leq x \leq 0.04$) in the angle range of $20^\circ \leq 2\theta \leq 90^\circ$.

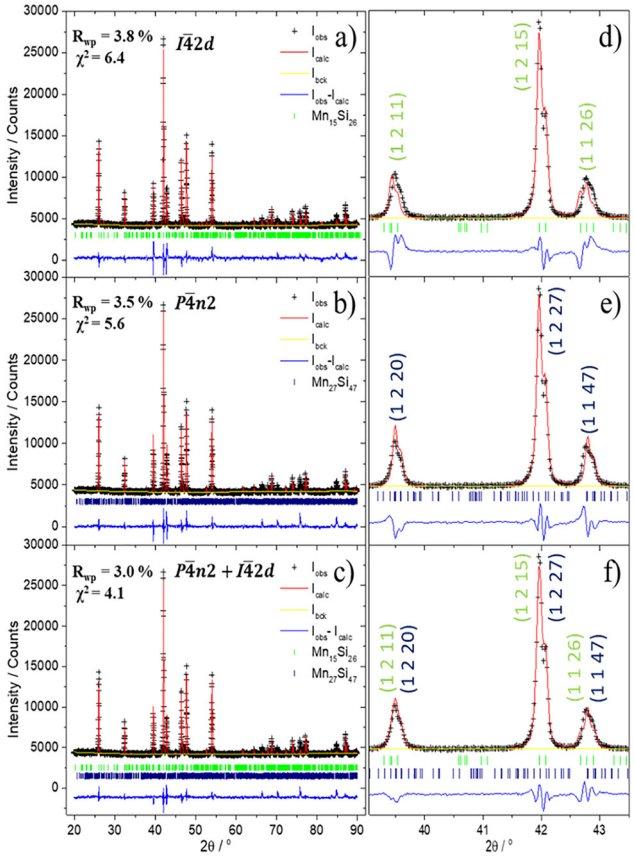

Fig. 3 Powder XRD Rietveld refinement profiles of $MnSi_{1.75}$ for three structural models: (a) single phase of $I\bar{4}2d$ $Mn_{15}Si_{26}$, (b) single phase of $P\bar{4}n2$ $Mn_{27}Si_{47}$ and (c) phase mixture of $P\bar{4}n2$ $Mn_{27}Si_{47}$ and $I\bar{4}2d$ $Mn_{15}Si_{26}$. (d)–(f) Refinement profiles focused on the peaks in the angular range $39^\circ \leq 2\theta \leq 43.5^\circ$. Final observed (black crosses), calculated (red solid line), calculated background (yellow line) and difference (blue line). Reflection positions for the $Mn_{27}Si_{47}$ and $Mn_{15}Si_{26}$ phases are marked in navy and green colours, respectively.

desired HMS phase without the detection of any impurities, secondary phases or unreacted reagents. Rietveld refinements were carried out to study the structural properties of the developed compounds. Initially, the investigations focused on the pristine phase, where Al atoms are not involved in the structure and the X-ray scattering factors of Mn and Si atoms present a good contrast. Investigating different commensurate models, the Rietveld analysis led to important conclusions. It must be noted here that during the refinements, the same process was followed and the same number of parameters related to the background and refinement profiles were considered, in order to extract reliable conclusions about the different structural models. In addition, the thermal parameters of all elements were fixed at the same value to minimize the number of refined parameters and avoid correlation problems.

Initially, the four basic structural models of the NCL phases were studied as single phases. Fig. 3a and b illustrate the Rietveld refinement profiles for the $I\bar{4}2d$ $Mn_{15}Si_{26}$ and $P\bar{4}n2$ $Mn_{27}Si_{47}$ phases, while SI, Fig. S1 and S2 present the remaining refinement profiles of the single phases $P\bar{4}c2$ Mn_4Si_7 and $P\bar{4}n2$ $Mn_{11}Si_{19}$, respectively. Rietveld refinements show that among the four structural models, the $I\bar{4}2d$ $Mn_{15}Si_{26}$ and $P\bar{4}n2$ $Mn_{27}Si_{47}$ phases best describe the obtained XRD pattern. As can be observed, there is a clear improvement in the fitting of the experimental data with the calculated profiles for the two larger superstructures with the R_{wp} and χ^2 values presenting an appreciable reduction. Although most of the peaks of the experimental data fit well with both single-phase models in Fig. 3a and b, notable mismatches are observed at the Bragg peaks located at the angles of 39.5°, 42° and ~42.8° (Fig. 3d and e). The highest Bragg peak at 42° originates from the Mn sub-lattice, while the peaks close to 39.5° and 42.8° are attributed to the satellite reflection and the Si sub-lattice, respectively, according to previous studies.[26,27] However, comparing the two structural models, $P\bar{4}n2$ $Mn_{27}Si_{47}$ exhibits a better fit with lower goodness of fit and weight profile residual values, and as a result it more effectively describes the crystal structure of HMS. Studying the HMS structure in our analysis as a single

 © 2025 The Author(s). Published by the Royal Society of Chemistry

Open Access Article. Published on 25 November 2025. Downloaded on 1/19/2026 10:11:12 PM.
This article is licensed under a Creative Commons Attribution 3.0 Unported Licence.

phase, the aforementioned results are in agreement with previous reports thus far, which showed that at room temperature and up to 800 °C, $Mn_{27}Si_{47}$ is the only stable phase for HMS compounds with a stoichiometry close to $MnSi_{1.75}$.[21,22] Another interesting observation in Fig. 3d and e is the fact that the intense differences in the two single-phase structural models with the experimental data at the Bragg peaks of 39.5° and 42.8° originate from opposite directions, and the weakness of the two models to reach the angle position of specific Bragg peaks. Conversely, the mismatch of the reflection position in both models at the highest Bragg peak of 42° is less noticeable.

Extending our investigations one step further and exploring the case of a phase mixture model between the two superstructures, $P\bar{4}n2$ $Mn_{27}Si_{47}$ and $I\bar{4}2d$ $Mn_{15}Si_{26}$, the refinement showed even better results with χ^2 = 4.1 and R_{wp} = 3.0% (Fig. 3c). The phase mixture model presents an impressive fitting of Bragg peaks at 39.5° and 42.8°, improving the reflection positions, while the fitting at the highest Bragg peak presents a less pronounced improvement. These important results led to the conclusion that the phase mixture model most effectively describes the crystal structure of the HMS phase mainly due to the displacement correction of the Bragg reflections, which come mainly from the [Si] sub-lattice. Table 1 presents the results from the Rietveld refinements for all the structural models investigated herein. The four NCL phases present similar values for the *a* lattice constant, while the *c* lattice constant increased with an increase in the number (*n*) of Mn sub-cells, as expected. The values derived by Rietveld analysis are in a good agreement with the results from previous studies.[15] The two-phase mixture model also exhibits lattice constant values close to those of the single-phase models. $Mn_{27}Si_{47}$ is the majority phase with a percent of 74.4 wt%.

Le Bail analysis was performed on the powder XRD data of the pristine phase using the GSAS-II software package for a direct comparison between the commensurate phase mixture model and the incommensurate (3 + 1)D approach. The Le Bail refinement of the incommensurate phase was carried using the superspace group $I4_1/amd(00\gamma)00ss$ and the lattice parameters from the study by Miyazaki *et al.*[25] as starting values. The two Le Bail refinement profiles are presented in Fig. S3 and S4 in the SI. As can be observed, the results are striking. Both calculated profiles present quite good fitting with the experimental data. The weight profile residual and goodness of fit of phase mixture almost reach the same levels as those of the incommensurate structural model which exhibits slightly better values. Le Bail analysis confirms the incommensurate nature of HMS phases, as shown in previous studies,[25–28,65] while in parallel it reveals a remarkable approximation for the commensurate two-phase mixture model, describing very well, almost equally with the incommensurate model, the structure of HMS. Moreover, it must be noted that the refined lattice parameters and modulation vector γ from the Le Bail refinement of the (3 + 1)D superspace group (Table S1) are in a very good agreement with the Le Bail study by Chauhan *et al.*[28] (for the pristine polycrystalline phase), confirming the validity of our analysis.

Using the two-phase mixture model, Rietveld refinements were performed for all the Al-doped phases in $Mn(Si_{1-x}Al_x)_{1.75}$ ($0.02 \leq x \leq 0.04$), following the same process and refining the same parameters. The refinement profiles of the Al-doped phases are shown in the SI. The phase mixture model provides a good fitting with the experimental data ($3 \leq \chi^2 \leq 4$, $3.0\% \leq R_{wp} \leq 4.2\%$), indicating that the Al atoms occupy the silicon sites in both phases. However, our structural investigations are not able to go further. Due to the similar X-ray scattering factors of silicon and aluminium as neighbouring elements, X-rays cannot provide sufficient contrast and information whether Al atoms show a preference among the crystallographic positions of silicon. Thus, it is assumed for simplicity of the refinement process that Al atoms equally occupy all silicon sites in both phases, $Mn_{27}Si_{47}$ and $Mn_{15}Si_{26}$, fixing their values to the nominal ones. Table 2 presents the refined lattice parameters of the phase mixture model, $P\bar{4}n2$ $Mn_{27}Si_{47}$ and $I\bar{4}2d$ $Mn_{15}Si_{26}$, for all the developed $Mn(Si_{1-x}Al_x)_{1.75}$ ($0.02 \leq x \leq 0.04$) materials. The substitution of Si with an Al atom causes structural changes in the two tetragonal superstructures, and also affects their phase fraction. A general reduction in wt% of the majority $Mn_{27}Si_{47}$ superstructure for all the Al-doped phases is observed in comparison with the pristine phase. Al atoms seem to enhance the partial transition of $Mn_{27}Si_{47}$ to $Mn_{15}Si_{26}$. $Mn_{15}Si_{26}$ becomes the majority phase for the cases of x = 0.025 and 0.03. Fig. 4 presents the evolution of lattice parameters as a function of Al composition. As can be observed, there is an increase in the *c* lattice constant with an increase in Al content in both phases. Conversely, Al substitution does not cause any significant effect in the *a* lattice constant in both superstructures,

Table 1 Results from Rietveld refinements of powder XRD data of pristine phase with the nominal stoichiometry of $MnSi_{1.75}$ for different commensurate structural models of the NCL phases

Single phase	Space group	*a*/Å	*c*/Å	*V*/Å^3	χ^2	R_{wp}/%
Mn_4Si_7	$P\bar{4}c2$	5.52436(8)	17.4581(5)	532.80(2)	12.4	5.3
$Mn_{11}Si_{19}$	$P\bar{4}n2$	5.5258(1)	48.015(2)	1466.12(7)	22.4	7.1
$Mn_{15}Si_{26}$	$I\bar{4}2d$	5.52558(6)	65.480(1)	1999.22(4)	6.4	3.8
$Mn_{27}Si_{47}$	$P\bar{4}n2$	5.52497(5)	117.863(2)	3597.8(1)	5.6	3.5
Phase mixture	**wt%**	***a*/Å**	***c*/Å**	***V*/Å^3**	**χ^2**	**R_{wp}/%**
$Mn_{27}Si_{47}$	74.4(2)	5.527(1)	117.924(4)	3602.3(1)	4.1	3.0
$Mn_{15}Si_{26}$	25.6(6)	5.5268(2)	65.461(2)	1999.5(2)		

Open Access Article. Published on 25 November 2025. Downloaded on 1/19/2026 10:11:12 PM.
This article is licensed under a Creative Commons Attribution 3.0 Unported Licence.

Table 2 Refined parameters from powder XRD Rietveld refinements of the $Mn(Si_{1-x}Al_x)_{1.75}$ phases ($0.02 \leq x \leq 0.04$) for the commensurate phase mixture approximation

	$Mn_{27}Si_{47}$				$Mn_{15}Si_{26}$			
x	wt%	a/Å	c/Å	V/Å^3	wt%	a/Å	c/Å	V/Å^3
0.02	66.9(4)	5.5285(2)	117.976(5)	3605.8(2)	33.1(7)	5.5259(2)	65.468(3)	1999.1(2)
0.025	42.0(4)	5.5284(3)	117.995(1)	3606.3(4)	58.0(2)	5.52750(7)	65.572(1)	2003.4(1)
0.03	42.8(6)	5.5294(3)	118.057(8)	3609.5(3)	57.2(4)	5.5271(1)	65.522(2)	2001.6(1)
0.04	52.0(6)	5.5290(2)	118.138(6)	3611.5(2)	48.0(7)	5.5327(4)	65.612(6)	2008.5(3)

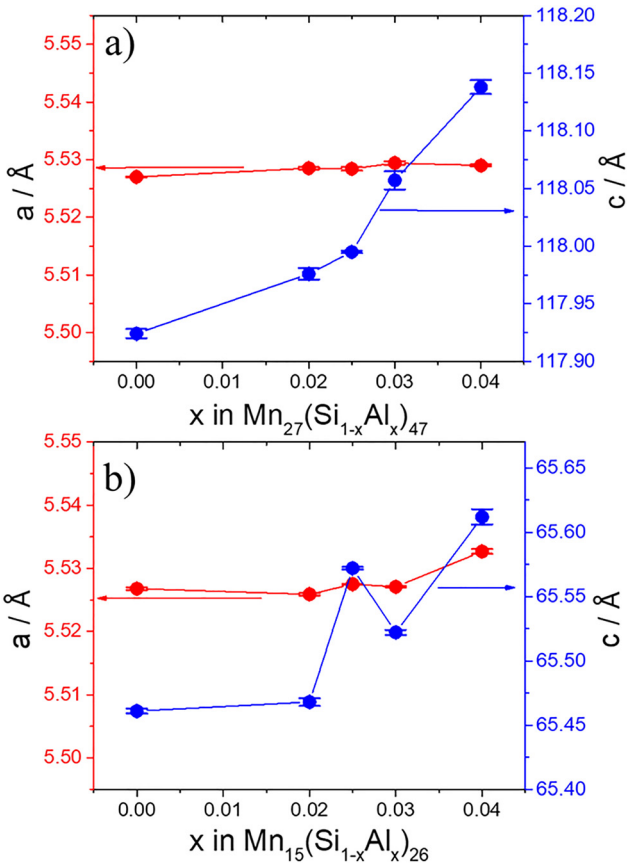

Fig. 4 Refined lattice constants as a function of Al content for the two NCL phases of (a) $Mn_{27}(Si_{1-x}Al_x)_{47}$ ($0 \leq x \leq 0.04$) and (b) $Mn_{15}(Si_{1-x}Al_x)_{26}$ ($0 \leq x \leq 0.04$), derived from the powder XRD Rietveld refinements of the phase mixture model.

remaining almost stable with an increase in Al content. This is quite logical given that the lattice parameter along the x and y directions only depends on the Mn sub-lattice, not on the Si sub-lattice where chemical substitution takes place. The increase in c lattice parameter in both tetragonal phases with an increase in Al content originates from the substitution of silicon atoms (r_{Si} = 111 pm) with the slightly larger aluminum atoms (r_{Al} = 118 pm), which causes expansion of the [Si] sub-lattice, and consequently an overall expansion in the superstructures along the z axis. As a result, the unit cell volume increased slightly for the Al-doped phases compared with the pristine one (Table 2). The expansion of the [Si] sub-lattice with Al doping may be correlated with the reinforcement of the partial phase transition. This hypothesis can be supported by the fact that an analogous increase in the unit cell volume, which is due to the thermal expansion at high temperatures, causes the same phase transition from $Mn_{27}Si_{47}$ to $Mn_{15}Si_{26}$.[21] Allam *et al.* suggested that a displacement type is responsible for this phase transition. The enhancement in partial phase transition observed here may originate from an analogous displacement, which takes place in Si sub-lattice, due to the substitution of Si atoms by the larger Al atoms. Another possible explanation could be that Al atoms may cause a type of disorder in the $Mn_{27}Si_{47}$ superstructure, which consequently favours the partial transition to the $Mn_{15}Si_{26}$ phase. In addition, the correlation of the partial phase transition with the expansion of the [Si] sub-lattice seems to be in agreement with the superspace approach reported by Chauhan *et al.*, which showed that the enlargement of c_{Si} with Al substitution reduces γ.[28] Taking into account the γ values of the two phases, $Mn_{27}Si_{47}$ (γ = 1.74) and $Mn_{15}Si_{26}$ (γ = 1.73), as well as the wt% ratios derived by the quantitative analysis of the phase mixture model, the overall γ was estimated across the $Mn(Si_{1-x}Al_x)_\gamma$ ($0 \leq x \leq 0.04$) series. Fig. 5 presents the calculated overall γ as a function of Al content compared with γ derived in the study by Chauhan *et al.* for the polycrystalline samples.[28] Interestingly,

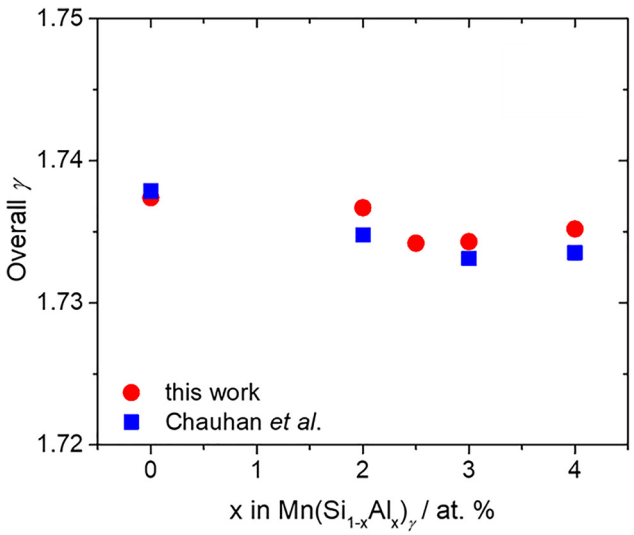

Fig. 5 Calculated overall γ (red spheres) across the $Mn(Si_{1-x}Al_x)_\gamma$ series derived by the quantitative Rietveld analysis of the phase mixture model as a function of Al content in comparison with the results obtained from the work of Chauhan *et al.* (blue squares).[28]

 © 2025 The Author(s). Published by the Royal Society of Chemistry

Open Access Article. Published on 25 November 2025. Downloaded on 1/19/2026 10:11:12 PM.
This article is licensed under a Creative Commons Attribution 3.0 Unported Licence.

there is very good agreement between the two studies, reaching values quite close to 1.736.[25,27] This indicates that the commensurate phase mixture approximates quite well the irrational z-axis ratio and modulation vector γ of the (3 + 1)D superspace group $I4_1/amd(00\gamma)00ss$, enhancing the validity of our approach across the $Mn(Si_{1-x}Al_x)_{1.75}$ ($0 \leq x \leq 0.04$) series.

Probably it is not random the fact that the phase mixture of the two larger NCL superstructures presents the best fitting results in our Rietveld analysis. The large number of crystallographic sites of the two superstructures seems to be able to describe the helical modulation of Si along the z-axis, resulting in a remarkable approximation of the modulated HMS structure, as shown by the Le Bail analysis. This is consistent with the superspace group approach in previous studies, which actually revealed the rotational modulation in the [Si] subsystem. As followed, the quantification of the two superstructures, $Mn_{15}Si_{26}$ and $Mn_{27}Si_{47}$, and the evolution of the phase fraction across the $Mn(Si_{1-x}Al_x)_{1.75}$ series ($0 \leq x \leq 0.04$) explain quite well the properties of the developed phases based on band structure calculations of the two commensurate phases.[29] Finally, another interesting feature that correlates the lattice expansion across the z axis with the partial phase transition from $Mn_{27}Si_{47}$ to $Mn_{15}Si_{26}$ can be observed in Fig. 4. A noticeable increase is observed in the c lattice constant for the $Mn_{15}Si_{26}$ superstructure, whereas $Mn_{27}Si_{47}$ shows a soft increase. The abnormal effect that takes place at $x = 0.025$ in the trend of the c lattice constant of $Mn_{15}Si_{16}$ may be correlated with the abrupt change in the fraction of two phases. Probably Al atoms do not equally occupy the Si sites in both superstructures, and their distribution in the Si sub-lattice may present fluctuations, showing a preference in $Mn_{27}Si_{47}$-rich regions. According to the previous hypothesis, the expansion and atomic displacement in the Si sub-lattice become more intense in these regions, favoring the transition to the $Mn_{15}Si_{26}$ phase with an appreciable increase in wt. ratio from ~33% to 58%. Finally, the accumulation of more Al atoms in the new phase, $Mn_{15}Si_{26}$, is denoted by the noticeable increase in the c lattice constant observed at $x = 0.025$. Neutron diffraction is considered to support future structural investigations, extracting possibly important information about the validation of phase mixture approximation and the distribution of Al atoms on the silicon sites of two superstructures. A neutron study may also give insight into the abrupt change in the phase fraction at $x = 0.025$, which seems to be correlated with the abnormal effect in the trend of the c lattice constant of the $Mn_{15}Si_{26}$ phase.

Electrical and thermal transport properties of $Mn(Si_{1-x}Al_x)_{1.75}$

After hot-press sintering, electrical and thermal transport property measurements were performed on the consolidated pellets and legs, which exhibited densities above 95% of the calculated values, as extracted by Rietveld analysis (Table S2). Fig. 6 presents the electrical conductivity, Seebeck coefficient and PF measurements as a function of temperature for the nominal $Mn(Si_{1-x}Al_x)_{1.75}$ ($0 \leq x \leq 0.04$) phases. As shown, the electrical conductivity of all the HMS phases is reduced as a function of temperature. This metallic-like behaviour confirms the degenerate nature of the $Mn_{27}Si_{47}$ and $Mn_{15}Si_{26}$ phases according to previous band structure calculations.[29] Both phases have similar band structures with a band gap of *ca.* 0.78 eV and can be treated as degenerated semiconductors, given that the Fermi level is located in the valence band (0.05–0.07 eV below the top of the valence band), separating it into occupied and unoccupied parts.[15,29] In addition, the evolution of the electrical conductivity of the pristine phase with temperature excludes the case of Mn_4Si_7, simultaneously verifying the results from

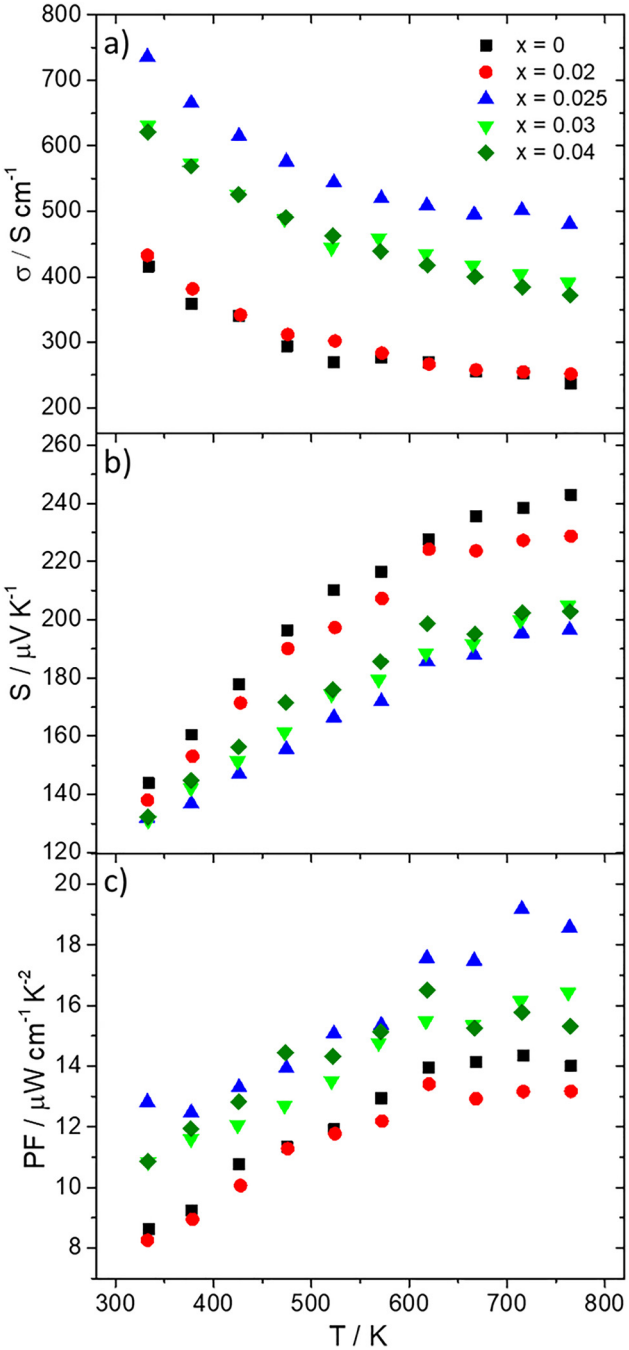

Fig. 6 (a) Electrical conductivity, (b) Seebeck coefficient and (c) PF as a function of temperature for the $Mn(Si_{1-x}Al_x)_{1.75}$ phases ($0 \leq x \leq 0.04$).

Open Access Article. Published on 25 November 2025. Downloaded on 1/19/2026 10:11:12 PM.
This article is licensed under a Creative Commons Attribution 3.0 Unported Licence.

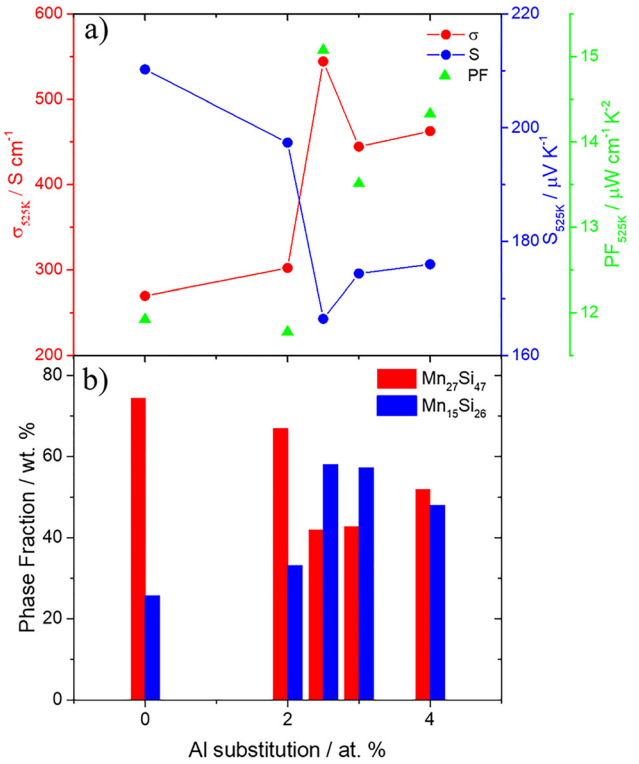

Fig. 7 (a) Electrical conductivity, Seebeck coefficient and PF at a constant temperature of 525 K as a function of Al substitution and (b) evolution of phase fraction of two phases, $Mn_{27}Si_{47}$ and $Mn_{15}Si_{26}$, with Al substitution, as derived from the Rietveld refinements.

the Rietveld refinements because this NCL phase presents semiconducting behaviour.[29] Al substitution has an appreciable impact on the electrical transport properties of the investigated materials. A significant increase in electrical conductivity is observed for the Al-doped phase with $x = 0.025$, while for $x > 0.025$ a smooth decrease takes place. The Seebeck coefficient data present positive values for all the HMS phases, denoting p-type behaviour. All the Al-doped phases present a reduction in Seebeck coefficient in comparison with the pristine material, indicating an increase in hole concentration. In Fig. 7a, it is obvious that Al substitution causes effective hole doping, tuning the electrical transport properties and optimizing the PF in the $Mn(Si_{1-x}Al_x)_{1.75}$ ($0 \leq x \leq 0.04$) series. According to the rule of valence electron count (VEC), the substitution of Si by Al causes a gradual reduction in VEC below 14, shifting the Fermi level deeper inside the valence band and creating more unfilled orbitals.[28,66] Following the rule VEC = $7 + (4(1 - x) - 3x)\gamma$ for the $Mn(Si_{1-x}Al_x)_\gamma$ phases, we estimated the VEC separately for the two phases according to the phase mixture model (Table S3). 7, 4 and 3 represent the number of valence electrons of Mn, Si and Al, respectively. The sample with $x = 0.025$ presents the highest σ and lowest S values, implying that this phase exhibits the highest levels of hole concentration. 2.5% Al doping causes a reduction in VEC from 13.96 and 13.92 to 13.66 and 13.62 for $Mn_{27}Si_{47}$ ($\gamma = 1.74$) and $Mn_{15}Si_{26}$ ($\gamma = 1.73$), respectively.

The abrupt changes observed for $x = 0.025$ in both σ and S are quite noticeable (Fig. 7a). Conversely, smooth variations in electrical transport properties occur for either $x < 0.025$ or $x > 0.025$. These interesting features seem to be correlated with the structural changes observed previously in the Rietveld analysis. As shown in Fig. 7b, Al substitution favours the formation of $Mn_{15}Si_{26}$ in the phase mixture model. Interestingly, a notable change is also observed in the fraction of the two phases from $x = 0.02$ to 0.025. The ratio of $Mn_{15}Si_{26}$ presents an abrupt increase from ~33 to 58 wt%, becoming the majority phase, while for $x < 0.025$ and $x > 0.025$, a smooth variation is observed, analogous with that of electrical conductivity. Therefore, comparing Fig. 7a and b, the changes in the fraction of the two phases across the $Mn(Si_{1-x}Al_x)_\gamma$ ($0 \leq x \leq 0.04$) series seem to be correlated with the variation in carrier concentration in the system. This is also reflected by the overall trend of γ in Fig. 5. The overall reduction in γ of the phase mixture follows the trend of an increase in hole concentration. This is in agreement with the VEC rule and previous studies.[28,67] It is suggested here that the partial phase transition due to Al substitution probably affects the number of charge carriers, contributing to the increase in hole density for the $Mn_{15}Si_{26}$-rich phases. This suggestion is in agreement with the literature based on theoretical and experimental results for the hole concentration of two specific phases.[17,29,68] The calculations reported by Migas *et al.* show that the pristine $Mn_{15}Si_{26}$ exhibits higher levels of hole concentration (2.0×10^{21} cm^{-3}) than that of $Mn_{27}Si_{47}$ (1.1×10^{21} cm^{-3}).[29] Thus, when $Mn_{15}Si_{26}$ becomes the majority phase, it seems to contribute more strongly to the total number of charge carriers in the phase mixture, enhancing the hole concentration of the materials. The VEC estimations obtained for the pristine and Al-doped phases also agree with this suggestion. Due to the difference in γ of the two HMS phases, the VEC of $Mn_{15}Si_{26}$ presents lower values than that of $Mn_{27}Si_{47}$, indicating more unfilled orbitals in its valence band, and consequently creating a higher number of holes.

The significant increase in electrical conductivity surpasses the reduction in Seebeck coefficient, resulting in an improvement in PF for the Al-doped phases with $x \geq 0.025$. The optimization of PF is accomplished for the sample with 2.5% Al doping. At 715 K, $Mn(Si_{0.975}Al_{0.025})_{1.75}$ reaches the maximum PF of 19.2 μW cm^{-1} K^{-2}, which corresponds to an increase of *ca.* 34% compared to the pristine phase. Interestingly, comparing our data with that reported by Chauhan *et al.*,[28] an analogous trend is observed for the electrical transport properties of the polycrystalline HMS phases prepared by melt-spinning and SPS. A significant increase in electrical conductivity is also observed in the $Mn(Si_{1-x}Al_x)_{1.74}$ ($0 \leq x \leq 0.04$) series. Optimization of the TE properties is realized for $x = 0.03$, which is quite close to the optimum Al doping in this work.

Fig. 8 shows the total (κ_{tot}) thermal conductivity measurements as well as the lattice (κ_{lat}) and electronic (κ_{el}) contributions as a function of temperature. The electronic contribution is estimated using the Wiedemann–Franz law: $\kappa_{el} = L \times \sigma \times T$. The Lorenz number ($L$) is calculated using Fermi–Dirac statistics and the Seebeck coefficient data, considering scattering

 © 2025 The Author(s). Published by the Royal Society of Chemistry

Open Access Article. Published on 25 November 2025. Downloaded on 1/19/2026 10:11:12 PM.
This article is licensed under a Creative Commons Attribution 3.0 Unported Licence.

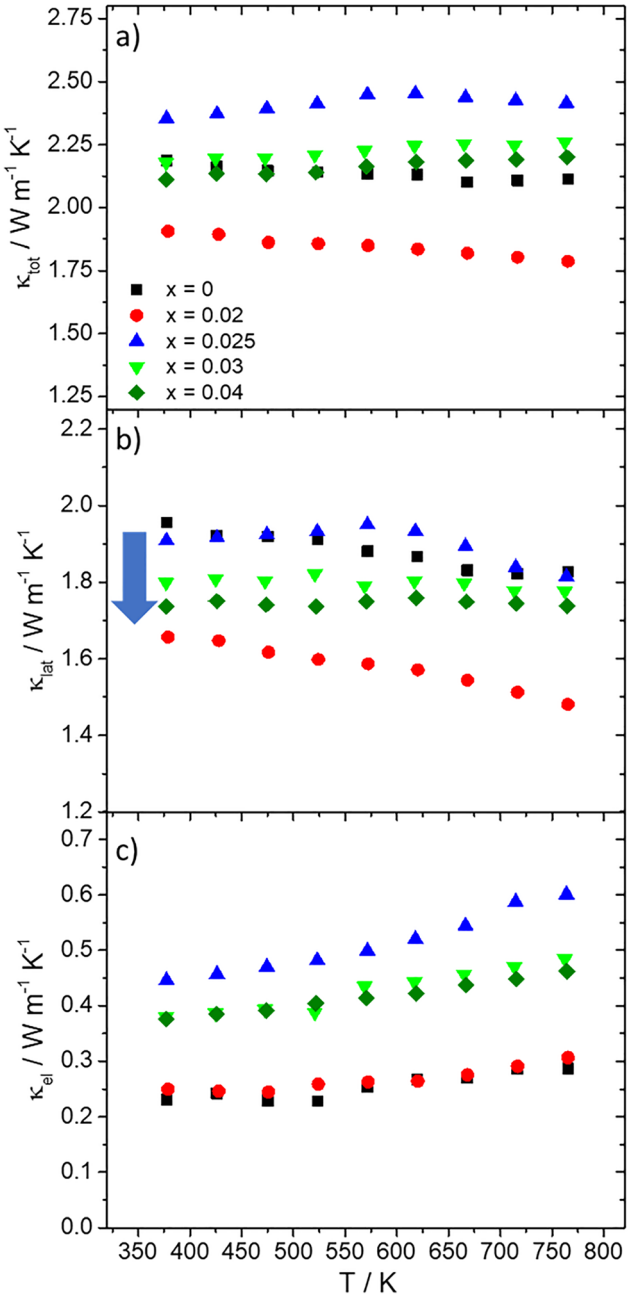

Fig. 8 (a) Total (κ_{tot}), (b) lattice (κ_{lat}) and (c) electronic (κ_{el}) thermal conductivity as a function of temperature for the $Mn(Si_{1-x}Al_x)_{1.75}$ phases ($0 \leq x \leq 0.04$).

from acoustic phonons.[69,70] The lattice thermal conductivity (κ_{lat}) is determined subtracting the electronic contribution from the total thermal conductivity ($\kappa_{tot} - \kappa_{el}$). As shown, the Al-doped phases with $x \geq 0.025$ present a small increase in total thermal conductivity, which comes from the enhanced electronic contribution of these materials. As expected, the electronic contribution follows the trend of electrical conductivity with the highest values observed for the 2.5% Al-doped phase. Conversely, a favourable reduction in the lattice thermal conductivity is observed for the Al-doped phases compared with the pristine compound. Taking into account the small difference in the atomic mass of Si and Al, we cannot conclude with certainty that the decrease in κ_{lat} comes from the mass fluctuations occurring in the lattice due to Al substitution. The reason for the reduction in κ_{lat} may be correlated with the structural changes observed in the Rietveld analysis. As shown previously, the substitution of Si by Al enhances the partial phase transition from $Mn_{27}Si_{47}$ to $Mn_{15}Si_{26}$, which may come from atomic displacement or type of disorder in the Si sub-lattice. The increase in $Mn_{15}Si_{26}$ wt% in the phase mixture model may enhance the structural complexity in the Al-doped phases and the mechanisms of phonon scattering. Among the Al-doped phases, the lowest κ_{lat} values are exhibited by the composition with $x = 0.02$, which presents an $Mn_{27}Si_{47}:Mn_{15}Si_{26}$ ratio of *ca.* 2 : 1. A similar reduction in κ_{lat} with Al substitution was also observed in the study by Luo *et al.*, where $Mn(Al_xSi_{1-x})_{1.80}$ phases were prepared by melt-spinning and SPS.[30]

Taking into account the aforementioned TE property measurements, the TE figure-of-merit was determined for $Mn(Si_{1-x}Al_x)_{1.75}$ ($0 \leq x \leq 0.04$) (Fig. 9). As can be observed, Al doping enhances the TE efficiency of the materials, with the maximum values exhibited for the case of $x = 0.025$. In the case of the compositions with $x > 0.025$, a gradual decrease in *ZT* is observed, denoting that tuning of the electrical transport properties and optimization of the TE performance were achieved through Al doping. It is obvious for $x = 0.025$ that the effective enhancement in PF due to the significant increase in electrical conductivity results in an improvement in the TE figure-of-merit, reaching the maximum value close to 0.6 at 773 K.

Recycled Si kerf-based $Mn(Si_{0.975}Al_{0.025})_{1.75}$ phases synthesized by arc melting

To utilize recyclable Si for the development of silicide thermoelectrics, here we also attempted to replace high-purity Si with

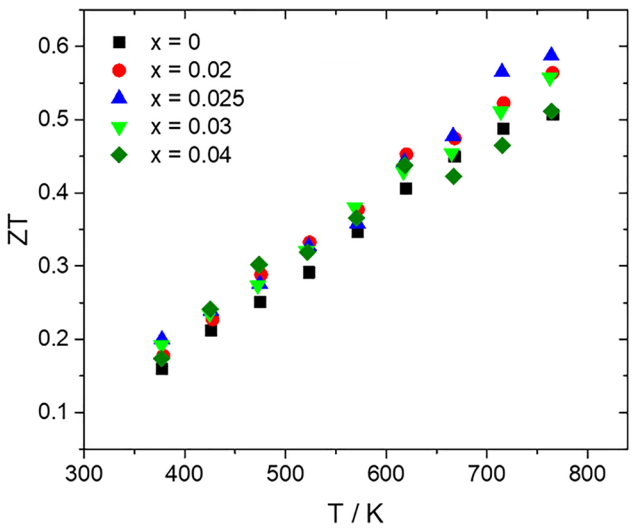

Fig. 9 *ZT* as a function of temperature for the $Mn(Si_{1-x}Al_x)_{1.75}$ phases ($0 \leq x \leq 0.04$).

Open Access Article. Published on 25 November 2025. Downloaded on 1/19/2026 10:11:12 PM.
This article is licensed under a Creative Commons Attribution 3.0 Unported Licence.

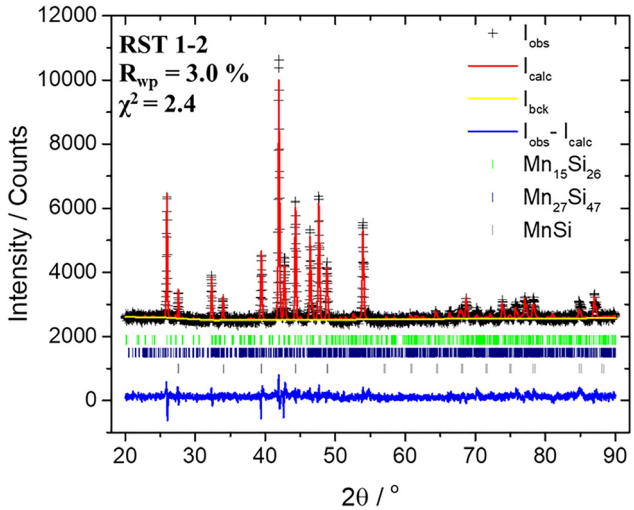

Fig. 10 Powder XRD Rietveld refinement profile of $Mn(Si_{0.975}Al_{0.025})_{1.75}$ based on RST 1–2 silicon kerf for the phase mixture structural model. Final observed (black crosses), calculated (red solid line), calculated background (yellow line) and difference (blue line). Reflection positions for the $Mn_{15}Si_{26}$, $Mn_{27}Si_{47}$ and MnSi phases are marked with green, navy and gray colors, respectively.

recycled Si kerf from PV manufacturing. Two types of Si kerf were used with the codes RST 1–2 and RTS ODIN-0821. The two kerfs come from the slicing process of Si wafers. The characterization results are reported in detail in our previous study.[61] Small amounts (in ppm) of elemental impurities such as Al, Ca and Ni are identified in both kerfs, with the RST 1–2 kerf exhibiting slightly less amounts due to its different purification procedure from that of RST ODIN-0821. In addition, a thin silicon oxide layer was detected on the surface of the silicon kerf nanoparticles, which is unavoidable during the purification process. The two Si kerf-based materials with the nominal stoichiometry $Mn(Si_{0.975}Al_{0.025})_{1.75}$ were developed by the arc melting method, following the same process as previously reported. The optimum amount of Al doping was implemented to enhance the performance of the materials according to the previous results. Powder XRD confirmed the desired HMS phase. However, an appreciable amount of secondary phase MnSi was also detected in both Si kerf-based products. Rietveld analysis was performed to quantify the multiple phases and extract information about the crystal structure of the materials. The refinements were executed as previously reported, implementing the two-phase mixture model for the HMS phase and following the same refinement process. Fig. 10 presents the Rietveld refinement profile of the RST 1–2 kerf-based product, while the profile of the RST ODIN-0821 kerf case is shown in Fig. S9. As can be observed, the calculated phase mixture model fits quite well with the experimental data (R_{wp} = 3.0% and $2.3 \leq \chi^2 \leq 2.4$). The existence of MnSi is clearly obvious with the characteristic Bragg peaks at 44.3° and 48.8°. Table S4 in the Supplementary Information presents the refined parameters extracted by the Rietveld analysis of two Si kerf-based compounds. Both kerf-based products present similar phase ratios for the HMS mixture model as well as for the secondary phase. $Mn_{27}Si_{47}$ is the majority phase with a percent just above 50 wt%, while $Mn_{15}Si_{26}$ is close to ∼30 wt%. The lattice constants of both phases present similar values with that of their Si-5N counterpart. The presence of relatively high amounts of MnSi, about 20 wt%, will have a strong impact in their TE properties, as shown later.

Backscattering SEM imaging was performed on the surface of the developed pellets to investigate the microstructure of the kerf-based materials in comparison with their Si-5N counterpart (Fig. 11). The differences in the backscattering SEM imaging are quite distinctive between the Si-5N and kerf-based samples. The secondary phase, MnSi, is clearly noticeable in the microstructure of both kerf-based materials, confirming the powder XRD data. A large number of light-gray spots with various sizes denote the existence of MnSi in appreciable amounts, while the dark-grey matrix corresponds to the HMS phases. Alternatively, Fig. 11a shows an almost clear microstructure with a homogeneous colour, indicating

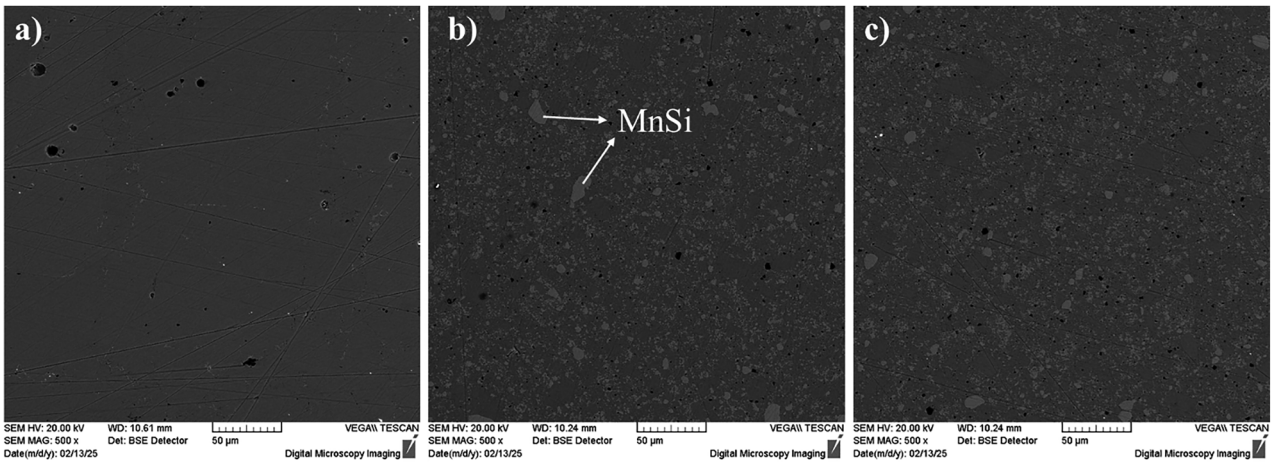

Fig. 11 Backscattering SEM images for the $Mn(Si_{0.975}Al_{0.025})_{1.75}$ phases based on (a) Si-5N, (b) RST 1–2 and (c) RST ODIN-0821. The scale bar in these images is 50 μm.

 © 2025 The Author(s). Published by the Royal Society of Chemistry

Open Access Article. Published on 25 November 2025. Downloaded on 1/19/2026 10:11:12 PM.
This article is licensed under a Creative Commons Attribution 3.0 Unported Licence.

the relatively good purity levels of the Si-5N product. However, slight traces of MnSi are also identified in the Si-5N product, which were not distinguished previously by powder XRD due to its very low amounts. This is characteristic in HMS phases given that the existence of slight amounts of MnSi precipitates has also been confirmed by SEM in a previous study, while they are also not detected by XRD.[30]

High-density pellets were fabricated implementing the same hot-press sintering conditions as previously reported. However, it must be noticed here that the two kerf-based pellets exhibit higher densities than that of the Si-5N samples. This originates from the formation of MnSi, which presents a higher density ($\sim$5.79 g cm^{-3}) than that of the HMS phases. Due to this reason, both the theoretical and experimental densities of the kerf-based pellets present higher values in Table S2. Fig. 12 presents the electrical transport property measurements of the two kerf-based materials compared with their Si-5N counterpart. As can be observed, the two kerf-based phases, in general, exhibit similar electrical conductivity values with that of the Si-5N case across the whole temperature range. A small increase is observed for the RST 1–2 case for temperatures up to 550 K. Conversely, the Seebeck coefficient is reduced significantly for the two kerf-based cases, indicating an appreciable increase in carrier concentration. It is obvious that the increased percentage of MnSi in the kerf-based materials is responsible for the increase in hole density and the sharp reduction in the Seebeck coefficient. This results in a decrease in PF for the two kerf cases in comparison with that of the high-purity case. However, it must be noted that the RST 1–2 case exhibits slightly higher PF values at high temperatures due to the improved electrical conductivity. The two kerf-based compounds present similar S values, denoting similar hole density levels. This is related to the fact that both kerf cases present almost the same MnSi ratios (19.9(1) and 19.6(2) wt%), according to the Rietveld analysis. As a result, the contribution of MnSi to the total hole concentration of the two kerf-based systems seems to be at the same levels. However, the increased hole concentration for the two kerf-based phases is not reflected with an increase in electrical conductivity, given that their values remain almost at the same levels with that of the Si-5N phase. Probably the reduction in hole mobility for the two kerf cases can explain this phenomenon. This reduction may come from the increased amounts of MnSi. Previous studies have shown that MnSi precipitates are responsible for an increase in carrier effective mass (m^*).[54,55] According to the single parabolic band (SPB) model, an increase in m^* can cause a reduction in hole mobility.[54] Similar conclusions about the effect of MnSi on the hole mobility were reported by Liu *et al.*, where the increase in hole mobility is attributed to the reduction in m^*, which comes from the suspension of MnSi phase.[54] Fig. 13 shows the thermal conductivity data as well as the lattice and electronic contributions estimated by the Wiedemann–Franz law, as previously reported. Both kerf-based materials present a significant increase in κ_{tot} in comparison with that of the Si-5N case, coming exclusively from κ_{lat}, which is the determinant contribution in κ_{tot}. As also shown in previous studies,[54,55,64]

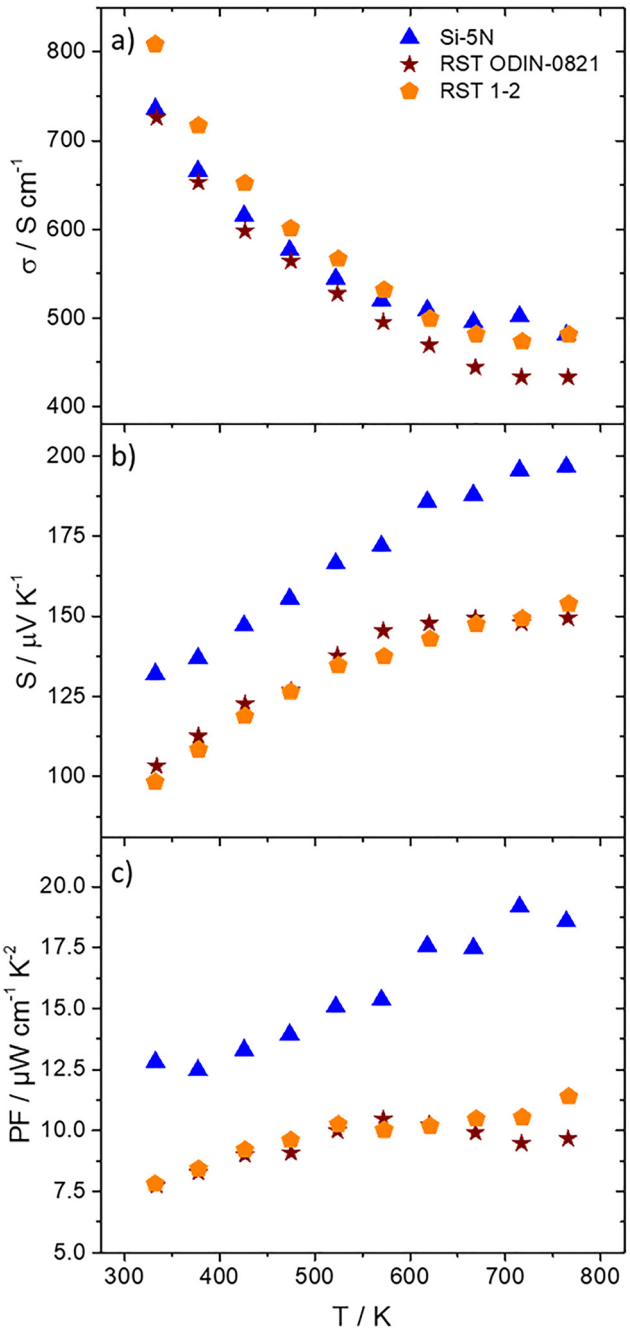

Fig. 12 (a) Electrical conductivity, (b) Seebeck coefficient and (c) PF as a function of temperature for the $Mn(Si_{0.975}Al_{0.025})_{1.75}$ phases based on Si-5N and the two Si kerfs, RST ODIN-0821 and RST 1–2.

the increased percentage of MnSi is detrimental for this noticeable increase in κ_{lat}, given that MnSi exhibits high levels of κ_{lat} compared to the HMS phases.[71]

Fig. 14 shows the TE figure-of-merit determined by the aforementioned TE property measurements. As can be observed, there is an appreciable reduction in efficiency for the two kerf-based materials. Both the decrease in PF and the increase in thermal conductivity contribute to the decline in ZT for the two kerf cases. However, the RST 1–2 case presents slightly higher ZT

Open Access Article. Published on 25 November 2025. Downloaded on 1/19/2026 10:11:12 PM.
This article is licensed under a Creative Commons Attribution 3.0 Unported Licence.

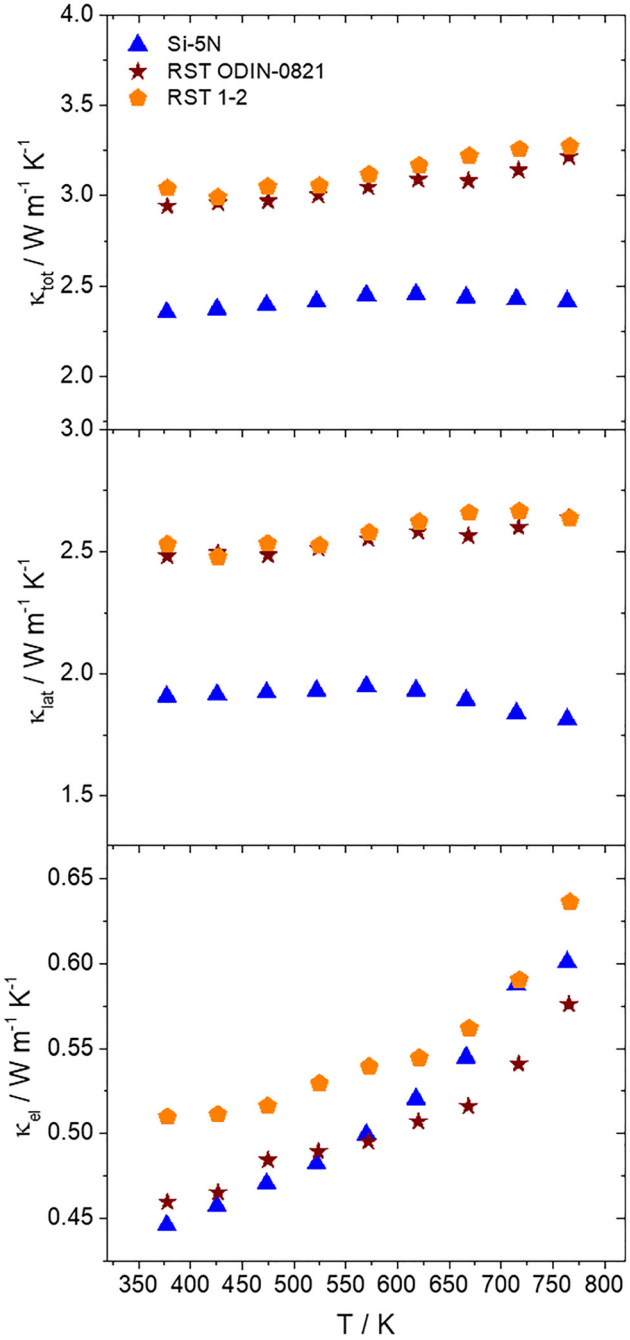

Fig. 13 Total (κ_{tot}), lattice (κ_{lat}) and electronic (κ_{el}) thermal conductivities as a function of temperature for the $Mn(Si_{0.975}Al_{0.025})_{1.75}$ phases based on Si-5N and the two Si kerfs, RST ODIN-0821 and RST 1–2.

at high temperatures than that of RST ODIN-0821 with a maximum value of 0.27 due to the improved PF. Obviously, the increased percentages of MnSi detected in both materials have a severe impact on their TE performance. The large amounts of MnSi presented in the kerf-based products seem to come from the appreciable Si loss that occurs during arc melting. The melting process was performed in the temperature range of 1500–2000 °C, just above the melting point of Si and below the boiling point of Mn. A possible explanation is that a reaction may take place in

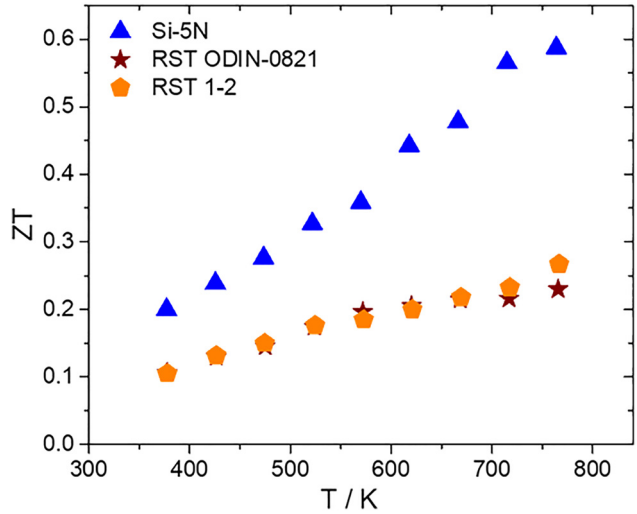

Fig. 14 *ZT* as a function of temperature for the $Mn(Si_{0.975}Al_{0.025})_{1.75}$ phases based on Si-5N and the two Si kerfs, RST ODIN-0821 and RST 1–2.

this temperature range between Si and SiO_2 to form SiO, which is subsequently evaporated. The presence of a thin SiO_2 layer (1–2 nm) on the surface of nano-grains of Si kerf was detected in our previous study implementing electron energy loss spectroscopy mapping in scanning transmission electron microscopy mode.[61] However, it must be noted that the arc melting is proven here to be an advantageous synthetic route in terms of product purity as well as TE properties in comparison with mechanical alloying (MA). Comparing the present results with those from our recent study on MA-based HMS phases,[64] it is obvious that the arc melting method exhibits products with higher purity, restricting the undesired MnSi phase and improving the TE properties of both the Si-5N- and kerf-based phases. It is notable that the amount of MnSi is reduced for the RST ODIN-0821-based product from 38 wt% to 19.6 wt% using the arc meting method, while the high-purity Si-based products eliminate MnSi. As a result, a sufficient improvement in PF and *ZT* is achieved for the arc melted phases. More research efforts should focus on the optimization of the purification and synthesis process for the two kerf cases to restrict the formation of further MnSi phases. Possibly, adding an excess amount of Si kerf at the beginning of the synthesis process may offset the lack of pure reagent element in the recycled material as well as its loss during the arc melting process, according to our previous hypothesis. This may favour the formation of the correct stoichiometry, $MnSi_{\gamma}$, mitigating the secondary phase, MnSi. Improving the TE properties of p-type kerf-based silicide thermoelectrics will enhance our attempts to fabricate more efficient silicide TE devices based on recycled silicon,[72] aiming to establish a circular economy approach in green energy technologies and an effective sustainable recycling solution in the PV industry.

Conclusions

In conclusion, HMS compounds with the nominal stoichiometry of $Mn(Si_{1-x}Al_x)_{1.75}$ ($0 \leq x \leq 0.04$) were prepared using the

 © 2025 The Author(s). Published by the Royal Society of Chemistry

Open Access Article. Published on 25 November 2025. Downloaded on 1/19/2026 10:11:12 PM.
This article is licensed under a Creative Commons Attribution 3.0 Unported Licence.

arc melting method and hot-press sintering. Structural investigations were performed executing powder XRD Rietveld refinements on structural models from the NCL phases. The Rietveld analysis revealed that the commensurate two-phase mixture approximation based on the $I\bar{4}2d$ $Mn_{15}Si_{26}$ and $P\bar{4}n2$ $Mn_{27}Si_{47}$ superstructures describes the experimental profile of the modulated crystal structure quite well. The majority phase for the pristine compound is $Mn_{27}Si_{47}$ with *ca.* 74.4 wt%. Le Bail analysis enhances the validity of our approximation, while in parallel it confirms the modulated structure of HMS using the (3 + 1)D superspace group $I4_1/amd(00\gamma)00ss$.

Al substitution in the Si sub-lattice induces structural changes in both superstructures and the phase fraction. An expansion across the z axis is observed in the tetragonal supercells due to the larger Al atoms, while the a lattice constant is affected marginally, given that it is dependent only on the Mn sub-cell. Interestingly, a variation in the phase mixture takes place across the $Mn(Si_{1-x}Al_x)_{1.75}$ ($0 \leq x \leq 0.04$) series. The enlargement in the [Si] sub-lattice due to Al substitution seems to favour the formation of the $Mn_{15}Si_{26}$ phase. At $x = 0.025$, a notable change occurs in the phase fraction, and $Mn_{15}Si_{26}$ becomes the majority phase with *ca.* 58 wt%. This structural change seems to be correlated with the abrupt changes in electrical transport properties observed at $x = 0.025$, possibly contributing positively to the increase in hole concentration. Al substitution causes effective hole doping, increasing the hole concentration. The 2.5% Al doped-phase exhibits a significant increase in electrical conductivity, appreciably enhancing the PF. This results in an improvement in ZT, reaching a maximum value close to 0.6 at 773 K.

In an attempt to utilise recycled Si kerf from the PV industry, two types of Si kerf with the codes RST 1–2 and RST ODIN-0821 were used as reagent elements for the synthesis of 2.5% Al-doped HMS phases. Powder XRD confirms the two HMS phases, while an appreciable amount of MnSi is also present in both kerf-based products with a ratio of *ca.* 20 wt%. The formation of MnSi is attributed to the loss of Si and the existence of SiO_2 in the two types of Si kerf. The metallic MnSi phase has a severe impact on the TE properties, reducing S and increasing κ_{lat}. As a result, the two kerf-based phases present lower efficiencies than that of their high-purity Si counterpart, reaching a maximum ZT of 0.27 at 773 K for the case of RST 1–2.

Conflicts of interest

There are no conflicts to declare.

Data availability

The authors confirm that the data supporting the findings of this study are available within the article and the supplementary information (SI). Supplementary information includes powder XRD Rietveld refinement profiles of remaining investigated phases, Le Bail refinement profiles of $MnSi_{1.75}$ for the commensurate phase mixture and the incommensurate structural model with the (3 + 1)D superspace group $I4_1/amd(00\gamma)00ss$. Refined lattice parameters and modulation vector results extracted from Le Bail refinement of incommensurate model are also included. Experimental and theoretical density values calculated by Rietveld analysis are included for the prepared materials as well as refined parameters from Rietveld refinements of kerf-based phases. Finally, estimations of Valence Electron Count (VEC) are presented for the two phases, $Mn_{27}Si_{47}$ and $Mn_{15}Si_{26}$, in the phase mixture model across the series $Mn(Si_{1-x}Al_x)_{1.75}$ ($0 \leq x \leq 0.04$). See DOI: https://doi.org/10.1039/d5ma00500k.

Raw data that support the findings of this study are available from the corresponding author upon reasonable request.

Acknowledgements

This project has received funding from the European Union's Horizon 2020 research and innovation programme under grant agreement No. 958365.

References

1 S. Twaha, J. Zhu, Y. Yan and B. Li, *Renewable Sustainable Energy Rev.*, 2016, **65**, 698–726.
2 L. E. Bell, *Science*, 2008, **321**, 1457–1461.
3 G. J. Snyder and E. S. Toberer, *Nat. Mater.*, 2008, **7**, 105–114.
4 C. Dames, *Scr. Mater.*, 2016, **111**, 16–22.
5 A. Kumar, S. Bano, B. Govind, A. Bhardwaj, K. Bhatt and D. K. Misra, *J. Electron. Mater.*, 2021, **50**, 6037–6059.
6 J. Mao, Z. Liu, J. Zhou, H. Zhu, Q. Zhang, G. Chen and Z. Ren, *Adv. Phys.*, 2018, **67**, 69–147.
7 T. Hendricks, T. Caillat and T. Mori, *Energies*, 2022, **15**, 7307.
8 Q. Yan and M. G. Kanatzidis, *Nat. Mater.*, 2022, **21**, 503–513.
9 L. Huang, Q. Zhang, B. Yuan, X. Lai, X. Yan and Z. Ren, *Mater. Res. Bull.*, 2016, **76**, 107–112.
10 A. Nozariasbmarz, A. Agarwal, Z. A. Coutant, M. J. Hall, J. Liu, R. Liu, A. Malhotra, P. Norouzzadeh, M. C. Oeztuerk, V. P. Ramesh and Y. Sargolzaeiaval, *Jpn. J. Appl. Phys.*, 2017, **56**, 5S1.
11 A. T. Burkov, *Phys. Status Solidi A*, 2018, **215**, 1800105.
12 S. Hébert, D. Berthebaud, R. Daou, Y. Bréard, D. Pelloquin, E. Guilmeau, F. Gascoin, O. Lebedev and A. Maignan, *J. Phys.: Condens. Matter*, 2016, **28**, 013001.
13 L. D. Zhao, J. He, C. I. Wu, T. P. Hogan, X. Zhou, C. Uher, V. P. Dravid and M. G. Kanatzidis, *J. Am. Chem. Soc.*, 2012, **134**, 7902–7912.
14 T.-R. Wei, C.-F. Wu, F. Li and J.-F. Li, *J. Materiomics*, 2018, **4**, 304–320.
15 W.-D. Liu, Z.-G. Chen and J. Zou, *Adv. Energy Mater.*, 2018, **8**, 1800056.
16 G. Kim, H. Shin, J. Lee and W. Lee, *Met. Mater. Int.*, 2021, **27**, 2205–2219.
17 I. Kawasumi, M. Sakata, I. Nishida and K. Masumoto, *J. Mater. Sci.*, 1981, **16**, 355–366.

Open Access Article. Published on 25 November 2025. Downloaded on 1/19/2026 10:11:12 PM.
This article is licensed under a Creative Commons Attribution 3.0 Unported Licence.

18 A. Teknetzi, E. Tarani, E. Symeou, D. Karfaridis, D. Stathokostopoulos, E. Pavlidou, T. Kyratsi, E. Hatzikraniotis, K. Chrissafis and G. Vourlias, *Ceram. Int.*, 2021, **47**, 243–251.
19 J. M. Higgins, A. L. Schmitt, I. A. Guzei and S. Jin, *J. Am. Chem. Soc.*, 2008, **130**, 16086–16094.
20 D. C. Fredrickson, S. Lee, R. Hoffmann and J. Lin, *Inorg. Chem.*, 2004, **43**, 6151–6158.
21 A. Allam, P. Boulet, C. A. Nunes, J. Sopousek, P. Broz and M.-C. Record, *J. Alloys Compd.*, 2013, **551**, 30–36.
22 A. Allam, C. A. Nunes, J. Zalesak and M.-C. Record, *J. Alloys Compd.*, 2012, **512**, 278–281.
23 A. Zhou, T. Zhu, X. Zhao and E. Mueller, *J. Mater. Res.*, 2011, **26**, 1900–1906.
24 L. M. Levinson, *J. Solid State Chem.*, 1973, **6**, 126–135.
25 Y. Miyazaki, D. Igarashi, K. Hayashi, T. Kajitani and K. Yubuta, *Phys. Rev. B:Condens. Matter Mater. Phys.*, 2008, **78**, 214104.
26 Y. Miyazaki, H. Hamada, H. Nagai and K. Hayashi, *Materials*, 2018, **11**, 926.
27 S. Le Tonquesse, L. Joanny, Q. Guo, E. Elkaim, V. Demange, D. Berthebaud, T. Mori, M. Pasturel and C. Prestipino, *Chem. Mater.*, 2020, **32**, 10601–10609.
28 N. S. Chauhan, I. Ono, K. Hayashi and Y. Miyazaki, *ACS Appl. Mater. Interfaces*, 2022, **14**, 51983–51993.
29 D. B. Migas, V. L. Shaposhnikov, A. B. Filonov, V. E. Borisenko and N. N. Dorozhkin, *Phys. Rev. B:Condens. Matter Mater. Phys.*, 2008, **77**, 075205.
30 W. Luo, H. Li, F. Fu, W. Hao and X. Tang, *J. Electr. Mater.*, 2011, **40**, 1233–1237.
31 D.-K. Shin, S.-W. You and I.-H. Kim, *J. Korean Phys. Soc.*, 2014, **64**, 1412–1415.
32 X. Xu, L. Xie, Q. Lou, M. He, B. Jiang, Y. Yu, D. Wu and J. He, *Appl. Phys. Lett.*, 2019, **115**, 123902.
33 S. Vivès, C. Navone, E. Gaudin and S. Gorsse, *J. Mater. Sci.*, 2017, **52**, 12826–12833.
34 D.-K. Shin, S.-C. Ur, K.-W. Jang and I.-H. Kim, *J. Electr. Mater.*, 2014, **43**, 2104–2108.
35 Q. Guo, W. Zhang, Z. Liu, X. Fu, S. Le Tonquesse, N. Sato, H.-W. Son, K. Shimamura, D. Berthebaud and T. Mori, *ACS Appl. Mater. Interfaces*, 2021, **13**, 8574–8583.
36 S. Le Tonquesse, V. Dorcet, L. Joanny, V. Demange, C. Prestipino, Q. Guo, D. Berthebaud, T. Mori and M. Pasturel, *J. Alloys Compd.*, 2020, **816**, 152577.
37 S. Ghodke, N. Hiroishi, A. Yamamoto, H. Ikuta, M. Matsunami and T. Takeuchi, *J. Electr. Mater.*, 2016, **45**, 5279–5284.
38 N. Parse, S. Tanusilp, W. Silpawilawan, K. Kurosaki and S. Pinitsoontorn, *J. Electr. Mater.*, 2020, **49**, 2726–2733.
39 S. A. Barczak, R. A. Downie, S. R. Popuri, R. Decourt, M. Pollet and J. W. G. Bos, *J. Solid State Chem.*, 2015, **227**, 55–59.
40 X. Chen, A. Weathers, D. Salta, L. Zhang, J. Zhou, J. B. Goodenough and L. Shi, *J. Appl. Phys.*, 2013, **114**, 173705.
41 V. Ponnambalam, D. T. Morelli, S. Bhattacharya and T. M. Tritt, *J. Alloys Compd.*, 2013, **580**, 598–603.
42 Z. Li, Z. Su, H. Zhang, Q. Wang, J. Wang, X. Qian, Q. Cao, Z. Ding, J.-F. Li and S. Wang, *J. Eur. Ceram. Soc.*, 2023, **43**, 4799–4807.
43 D. Y. Nhi Truong, D. Berthebaud, F. Gascoin and H. Kleinke, *J. Electr. Mater.*, 2015, **44**, 3603–3611.
44 T. Homma, T. Kamata, N. Saito, S. Ghodke and T. Takeuchi, *J. Alloys Compd.*, 2019, **776**, 8–15.
45 S. Ghodke, A. Yamamoto, H.-C. Hu, S. Nishino, T. Matsunaga, D. Byeon, H. Ikuta and T. Takeuchi, *ACS Appl. Mater. Interfaces*, 2019, **11**, 31169–31175.
46 A. Yamamoto, S. Ghodke, H. Miyazaki, M. Inukai, Y. Nishino, M. Matsunami and T. Takeuchi, *Jpn. J. Appl. Phys.*, 2016, **55**, 020301.
47 W. Luo, H. Li, Y. Yan, Z. Lin, X. Tang, Q. Zhang and C. Uher, *Intermetallics*, 2011, **19**, 404–408.
48 S. Muthiah, R. C. Singh, B. D. Pathak, P. K. Avasthi, R. Kumar, A. Kumar, A. K. Srivastava and A. Dhar, *Nanoscale*, 2018, **10**, 1970–1977.
49 G. Kim, H. J. Rim, K. H. Lee, J. W. Roh and W. Lee, *Ceram. Int.*, 2019, **45**, 19538–19541.
50 X. Chen, J. Zhou, J. B. Goodenough and L. Shi, *J. Mater. Chem. C*, 2015, **3**, 10500–10508.
51 M. Saminathan, J. Palraj, P. Wesley, M. Moorthy, Ravikirana and S. Perumal, *Mater. Lett.*, 2021, **302**, 130444.
52 A. J. Zhou, T. J. Zhu, X. B. Zhao, S. H. Yang, T. Dasgupta, C. Stiewe, R. Hassdorf and E. Mueller, *J. Electr. Mater.*, 2010, **39**, 2002–2007.
53 A. Neubauer, C. Pfleiderer, R. Ritz, P. G. Niklowitz and P. Böni, *Phys. B*, 2009, **404**, 3163–3166.
54 W.-D. Liu, X.-L. Shi, R. Moshwan, Q. Sun, L. Yang, Z.-G. Chen and J. Zou, *J. Mater. Chem. C*, 2019, **7**, 7212–7218.
55 L. Wen-Hui, L. Han, L. Ze-Bing and T. Xin-Feng, State Key Laboratory of Advanced Technology for Material Synthesis and Processing, Wuhan University of Technology, Wuhan 430070, China, *Acta Phys. Sin.*, 2010, **59**, 8783.
56 Y. Sadia, M. Elegrably, O. Ben-Nun, Y. Marciano and Y. Gelbstein, *J. Nanomater.*, 2013, **2013**, 701268.
57 Y. Sadia, Z. Aminov, D. Mogilyansky and Y. Gelbstein, *Intermetallics*, 2016, **68**, 71–77.
58 C. Garcés-Ayerbe, P. Rivera-Torres, I. Suárez-Perales and D. I. Leyva-de la Hiz, *Int. J. Environ. Res. Public Health*, 2019, **16**(5), 851.
59 S. Nakamura, Y. Mori and K. Takarabe, *JJAP Conf. Proc.*, 2015, **3**, 011202.
60 G. Mesaritis, E. Symeou, A. Delimitis, S. Oikonomidis, M. Jaegle, K. Tarantik, C. Nicolaou and T. Kyratsi, *J. Alloys Compd.*, 2019, **775**, 1036–1043.
61 P. Mangelis, A. Sousanis, G. Mesaritis, P. S. Ioannou, A.-K. Søiland, Y. Xu and T. Kyratsi, *ACS Appl. Electron. Mater.*, 2024, 2988–2998.
62 G. Mesaritis, E. Symeou, A. Delimitis, M. Constantinou, G. Constantinides, M. Jeagle, K. Tarantik and T. Kyratsi, *J. Alloys Compd.*, 2020, **826**, 153933.
63 P. Mangelis, P. S. Ioannou, A.-K. Soiland and T. Kyratsi, *ACS Appl. Energy Mater.*, 2025, **8**, 1783–1795.

 © 2025 The Author(s). Published by the Royal Society of Chemistry

Open Access Article. Published on 25 November 2025. Downloaded on 1/19/2026 10:11:12 PM.
This article is licensed under a Creative Commons Attribution 3.0 Unported Licence.

64 P. Mangelis, K. Georgiou, P. S. Ioannou, S. Hadjipanteli, A.-K. Søiland and T. Kyratsi, *Nanomaterials*, 2025, **15**, 1286.
65 Y. Miyazaki, H. Hamada, K. Hayashi and K. Yubuta, *J. Electr. Mater.*, 2017, **46**, 2705–2709.
66 W. Liu, K. Yin, Q. Zhang, C. Uher and X. Tang, *Nat. Sci. Rev.*, 2017, **4**, 611–626.
67 D. C. Fredrickson, S. Lee and R. Hoffmann, *Inorg. Chem.*, 2004, **43**, 6159–6167.
68 C. Krontiras, K. Promoni and M. Roilos, *J. Phys. D: Appl. Phys.*, 1988, **21**, 509–512.
69 M. Ioannou, G. S. Polymeris, E. Hatzikraniotis, K. M. Paraskevopoulos and T. Kyratsi, *J. Phys. Chem. Solids*, 2014, **75**, 984–991.
70 E. Symeou, M. Karyou, A. Delimitis, M. Constantinou, G. Constantinides, C. Nicolaou, I. Giapintzakis and T. Kyratsi, *J. Phys. Chem. Solids*, 2022, **161**, 110472.
71 J.-G. Cheng, F. Zhou, J.-S. Zhou, J. B. Goodenough and Y. Sui, *Phys. Rev. B:Condens. Matter Mater. Phys.*, 2010, **82**, 214402.
72 P. S. Ioannou, P. Mangelis, S. Hadjipanteli, M. Mina, A. K. Søiland, J. Giapintzakis and T. Kyratsi, *Mater. Today Energy*, 2025, **49**, 101855.